

Role of inclined threading dislocations in stress relaxation in mismatched layers

P. Cantu, F. Wu,^{a)} P. Waltereit, S. Keller, A. E. Romanov,^{b)} S. P. DenBaars,^{a)} and J. S. Speck^{a),c)}

Materials Department and Electrical and Computer Engineering Department, University of California, Santa Barbara, California 93106

(Received 13 December 2004; accepted 4 March 2005; published online 16 May 2005)

(0001)-oriented epitaxial wurtzite III-nitride layers grown on mismatched substrates have no resolved shear stress on the natural basal and prismatic slip planes; however, strained III-nitride layers may gradually relax. We report on the stress relaxation of $\text{Al}_{0.49}\text{Ga}_{0.51}\text{N}$ layers grown on nominally relaxed $\text{Al}_{0.62}\text{Ga}_{0.38}\text{N}$ buffer layers on sapphire. The reduction in elastic strain of the $\text{Al}_{0.49}\text{Ga}_{0.51}\text{N}$ was enhanced by Si doping which caused an increased surface roughness. Despite the Si doping, the films always sustained step-flow growth. The extent of relaxation of the $\text{Al}_{0.49}\text{Ga}_{0.51}\text{N}$ layer was determined by on-axis ω - 2θ scans of (0001) peaks and reciprocal space maps of inclined (off-axis) peaks. Cross-section and plan-view transmission electron microscopy studies showed that the threading dislocations in the $\text{Al}_{0.49}\text{Ga}_{0.51}\text{N}$ layer inclined from the [0001] direction towards $\langle 1\bar{1}00 \rangle$ directions by $\sim 15\text{--}25^\circ$, perpendicular to their Burgers vector ($\frac{1}{3}\langle 11\bar{2}0 \rangle$). These inclined threading dislocations have a misfit dislocation component and thus provide stress relief. The contribution of the dislocation inclination to the degree of relaxation has been formulated and the energy release has been determined for dislocation inclination in mismatched stressed layers. © 2005 American Institute of Physics. [DOI: 10.1063/1.1897486]

I. INTRODUCTION

Heteroepitaxial growth of semiconductor materials has been important for the past 30 years. While the choice of the growth substrate is dictated by the availability of bulk single crystals, cost, and functionality, the constraints on the material for deposition are completely determined by the application. Consequently, it is common to grow epitaxial layers on substrates with a lattice mismatch, therefore generating elastic strains and mechanical stresses in the deposited layer. The study of stressed layers has large technological implications. Elastic strains directly modify the electronic and optical properties of semiconductors. For example, in (Al,In,Ga)As-based laser diodes, the strain in the layers in the active region is tailored to reduce the transparency current density and increase the differential gain of the device.¹ As a second example, nearly half of the sheet charge in the two-dimensional electron gas that forms at the (Al,Ga)N/GaN interface is due to piezoelectric-induced fixed charges in the strained (Al,Ga)N layer. To optimize the design, performance, and reliability of devices that use lattice-mismatched materials, it is important to understand the details of stress generation and relaxation processes.

Biaxial stress is generated in mismatched epitaxial layers which grow in a two-dimensional mode (i.e., step flow or layer-by-layer growth). The most common mode of stress relaxation in mismatched layers is related to the formation of misfit dislocations (MDs) at the film/substrate interface. The

MDs are usually accompanied by threading dislocations (TDs) which extend through the film. For the (001) epitaxial growth of films with a zinc-blende (fcc) structure, MD formation is accomplished by the glide of TDs on the inclined slip planes;^{2,3} this is commonly observed because the biaxial stress in the film produces shear stresses on the inclined $\{111\}$ glide planes. However, for the (0001) growth of crystals with a hexagonal structure, e.g., the wurtzite nitride semiconductors, neither the $\{1\bar{1}00\}$ prismatic glide planes nor the (0001) basal glide plane has any shear stresses. Therefore, the motion of dislocations via glide is not possible on the easy slip systems for the (0001) planar growth of wurtzite layers.

Despite the absence of shear stresses on the basal or prism planes, stress relaxation of heteroepitaxial (0001) nitride films has been previously reported. For instance, Lee *et al.*⁴ used Raman scattering and x-ray diffraction (XRD) to analyze Si-doped GaN films and found that the residual compressive strain decreased with increased Si doping. Based on transmission electron microscopy (TEM) studies, Ruvimov *et al.* suggested that for moderate Si concentrations ($\sim 3 \times 10^{18} \text{ cm}^{-3}$) stress relief of GaN films was achieved by the formation of dislocations in the basal plane.⁵ Romano *et al.*, using XRD, Raman scattering, and curvature techniques, observed that increased Si doping of GaN thin films led to a change from compressive to tensile stress that eventually produced cracks in the films.⁶ The change in the strain state was not attributed to changes in the relaxed GaN lattice constant due to Si incorporation, but rather Romano *et al.* discussed the possible role that Si doping decreased the high-temperature GaN island size at coalescence and thus generated high tensile stresses in accordance with the models

^{a)}Also at JST/ERATO UCSB Group.

^{b)}Permanent address: A.F. Ioffe Physico-Technical Institute, 194021 St. Petersburg, Russia.

^{c)}Electronic mail: speck@mrl.ucsb.edu

of crystalline coalescence (see, for example, Refs. 7–9). We note, however, the Romano *et al.* observed cracking in the GaN films for cases where the Si doping was initiated with the high-temperature GaN growth (“B films” in their paper) or delayed until nominally 100 nm of high-temperature GaN was deposited (“A films” in their paper). Thus, it is unclear if the predominant effect of Si doping was due to a change in the high-temperature GaN island size. Sahonta *et al.* observed enhanced relaxation of GaN films grown compressively on $\text{Al}_{0.28}\text{Ga}_{0.72}\text{N}$ buffer layers.¹⁰ They observed the “bending over and lateral migration” of TDs that allowed for dislocation rearrangements which lead to misfit dislocation dipole formation. These rearrangements were proposed as the main cause of stress relaxation.

We have observed the stress relaxation of Si-doped (0001) $\text{Al}_{0.49}\text{Ga}_{0.51}\text{N}$ on $\text{Al}_{0.62}\text{Ga}_{0.38}\text{N}$ films,¹¹ and of (0001)-oriented AlGaN/AlGaN superlattices grown on $\text{Al}_{0.62}\text{Ga}_{0.38}\text{N}$ buffer layers.¹² The stress relaxation in both types of samples was proposed to be related to the development of surface roughness of the layers due to Si doping. In addition, TEM analysis showed that TDs had [0001] line directions in the underlying $\text{Al}_{0.62}\text{Ga}_{0.38}\text{N}$ buffer layer but nearly all TDs were inclined in the nominally compressive lower Al-content layer. The inclination of the TDs was in an orientation that the TDs had a misfit component that released compressive stress. We found good agreement between strain values obtained from both XRD and TEM experiments,¹¹ thus confirming that TD inclination was the main cause of stress relaxation. The inclination of TDs was not related to their glide but rather to an *effective dislocation climb* process that occurs at the film surface during growth and is unlikely related to any bulk diffusion processes. A preliminary model that described the critical conditions for dislocation inclination was developed.¹³ This model showed how the inclined TDs may contribute to stress relaxation.

In this paper we combine both experimental and theoretical analyses to present a detailed description of the glide-free mechanism for misfit stress relaxation observed for Si-doped $\text{Al}_{0.49}\text{Ga}_{0.51}\text{N}$ on $\text{Al}_{0.62}\text{Ga}_{0.38}\text{N}$ thin films.

II. EXPERIMENT

Si-doped $\text{Al}_{0.49}\text{Ga}_{0.51}\text{N}/\text{Al}_{0.62}\text{Ga}_{0.38}\text{N}$ layers were grown on *c*-plane sapphire substrates by low-pressure metal-organic chemical-vapor deposition (MOCVD). Trimethylgallium (TMG) and trimethylaluminum (TMA) were used as group-III precursors, while ammonia (NH_3) was the group-V precursor. Disilane ($\text{DiSi}=\text{Si}_2\text{H}_6$) was used for Si doping. The reactor pressure was kept constant at 100 Torr.

The buffer layer growth was carried out in a H_2 ambient using a normal two-step process, where the deposition of a 14-nm-thick $\text{Al}_{0.60}\text{Ga}_{0.40}\text{N}$ nucleation layer at 600 °C was followed by a 1- μm -thick $\text{Al}_{0.62}\text{Ga}_{0.38}\text{N}$ buffer layer grown at 1150 °C with TMG and TMA flows of 29.5 and 35.5 $\mu\text{mol}/\text{min}$, respectively. Afterwards, 200-nm-thick Si-doped $\text{Al}_{0.49}\text{Ga}_{0.51}\text{N}$ films were grown in a N_2 ambient on top of the buffer layer at 1150 °C, using a TMG flow of 10.5 $\mu\text{mol}/\text{min}$ and a TMA flow of 7.1 $\mu\text{mol}/\text{min}$. The NH_3 flow was kept constant at 45 mmol/min for both layers. All

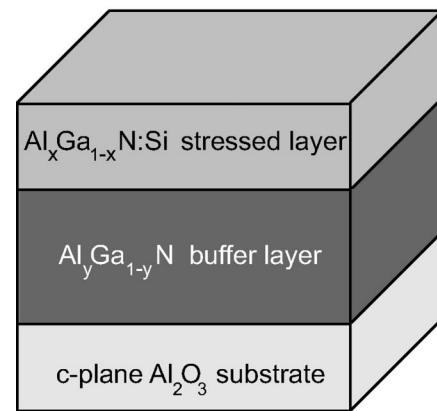


FIG. 1. Schematic of a stressed Si-doped $\text{Al}_{0.49}\text{Ga}_{0.51}\text{N}$ layer deposited on an $\text{Al}_{0.62}\text{Ga}_{0.38}\text{N}$ buffer layer. The Si-doped $\text{Al}_{0.49}\text{Ga}_{0.51}\text{N}$ layer was 200 nm thick and it grew compressively strained on top of a relaxed 1- μm -thick $\text{Al}_{0.62}\text{Ga}_{0.38}\text{N}$ buffer layer. The buffer layer itself was grown on a *c*-plane Al_2O_3 substrate.

structural studies showed that these layers grew in a step-flow mode. A schematic of the general sample structure is shown in Fig. 1.

A Si doping series was achieved by varying the DiSi flow rate during growth of the $\text{Al}_{0.49}\text{Ga}_{0.51}\text{N}$ layers between 1.25 and 8.57 nmol/min. This DiSi flow range resulted in Si concentrations from $[\text{Si}]=1.42 \times 10^{19} \text{ cm}^{-3}$ to $[\text{Si}]=9.72 \times 10^{19} \text{ cm}^{-3}$, as determined calibrate secondary-ion-mass spectroscopy data. Hereon, we refer to the Si doping in the layers as a Si to Al+Ga ratio, $\text{Si}/(\text{Al}+\text{Ga})$, where $\text{Si}/(\text{Al}+\text{Ga})=2 \times \text{DiSi flow}/(\text{TMG flow}+\text{TMA flow})$, ensuring variations between 7.1×10^{-5} and 4.9×10^{-4} for the samples under study.

The structural properties of the Si-doped $\text{Al}_{0.49}\text{Ga}_{0.51}\text{N}$ films were evaluated by atomic force microscopy (AFM) using a Digital Instruments Nanoscope III operated in tapping mode. High-resolution x-ray diffraction (HRXRD) experiments were performed on a Philips Materials Research diffractometer. TEM samples were prepared using tripod polishing and ion milling. The TEM studies were performed at 200 keV with both a JEOL 2000FX and a FEI T20 instruments.

III. RESULTS

A. AFM analysis of Si-doped $\text{Al}_{0.49}\text{Ga}_{0.51}\text{N}$ films: Si-induced surface roughness

The role of Si as an antisurfactant during growth of nitride films has been well documented. It has been shown that increasing $[\text{Si}]$ in GaN or AlGaN layers is related to the increased surface roughness of the films.^{14,15}

Figures 2(a) and 2(b) show $1 \times 1 \mu\text{m}^2$ AFM images of $\text{Al}_{0.49}\text{Ga}_{0.51}\text{N}$ films grown with $\text{Si}/(\text{Al}+\text{Ga})=7.1 \times 10^{-5}$ and $\text{Si}/(\text{Al}+\text{Ga})=4.9 \times 10^{-4}$, respectively. Figure 2(c) shows the dependence of the root-mean-square (rms) surface roughness on the $\text{Si}/(\text{Al}+\text{Ga})$ of the samples that showed the surface roughness increasing with $\text{Si}/(\text{Al}+\text{Ga})$. The rms surface roughness values obtained for the samples shown in Figs. 2(a) and 2(b) were 0.32 and 0.80 nm, respectively.

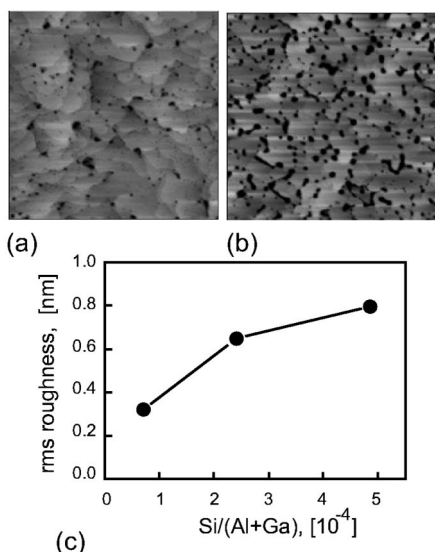


FIG. 2. Surface roughness analysis of Si-doped $\text{Al}_{0.49}\text{Ga}_{0.51}\text{N}$ films. (a) $1 \times 1 \mu\text{m}^2$ AFM image of a Si-doped $\text{Al}_{0.49}\text{Ga}_{0.51}\text{N}$ film grown using $\text{Si}/(\text{Al}+\text{Ga})=7.1 \times 10^{-5}$. (b) $1 \times 1 \mu\text{m}^2$ AFM image of a Si-doped $\text{Al}_{0.49}\text{Ga}_{0.51}\text{N}$ film grown using $\text{Si}/(\text{Al}+\text{Ga})=4.9 \times 10^{-4}$. (c) AFM root-mean-square (rms) surface roughness vs $\text{Si}/(\text{Al}+\text{Ga})$. The rms surface roughness values were 0.32 and 0.80 nm, for the samples shown in Figs. 2(a) and 2(b), respectively.

B. Observation of partial stress relaxation of Si-doped $\text{Al}_{0.49}\text{Ga}_{0.51}\text{N}$ films via HRXRD

X-ray ω - 2θ scans of the symmetric (0002) or (0004) reflections are commonly used to roughly determine the Al mole fraction of AlGaIn thin films. For the Si doping series we observed that the relative position of the $\text{Al}_{0.49}\text{Ga}_{0.51}\text{N}$ (0004) peak shifted closer to the $\text{Al}_{0.62}\text{Ga}_{0.38}\text{N}$ (0004) peak with increasing $\text{Si}/(\text{Al}+\text{Ga})$ in the films, as shown in Fig. 3(a). The change in the separation of the AlGaIn peaks was an indication that Si doping affected either the Al composition or the strain state of the $\text{Al}_{0.49}\text{Ga}_{0.51}\text{N}$ layers with respect to the $\text{Al}_{0.62}\text{Ga}_{0.38}\text{N}$ buffer layers. As symmetric scans in any reflection are not useful in determining both the composition and the strain state of thin films, we conducted reciprocal space maps (RSMs) to unambiguously determine both the strain and the Al composition of all layers.

X-ray RSMs were recorded near the $(10\bar{1}5)$ reflection in a coplanar geometry, i.e., the incident wave vector, the scattered wave vector, and the sample surface normal were all in the same plane, with shallow incidence of the x-ray beam in rocking curve mode using a 1.0-mm receiver slit. Figure 3(b) shows a RSM which includes the $(1,1,\bar{2},12)$ reflection of sapphire and the $(10\bar{1}5)$ reflections of the buffer and stressed layers, where the $(1,1,\bar{2},12)$ sapphire reflection, at $\theta_0 = 51.412^\circ$, and $\omega_0 = 26.946^\circ$, was used as angular reference. Using the known sapphire lattice constants, $a = 4.7588 \text{ \AA}$ and $c = 12.992 \text{ \AA}$, the in-plane (a) and out-of-plane (c) hexagonal cell dimensions of the AlGaIn layers were calculated from their respective values of θ and ω measured on the RSMs, allowing us to independently determine the Al composition and strain state of the films by using standard x-ray analysis. The degree of relaxation $R = 1 - (\varepsilon_{\text{meas}}/\varepsilon_{\text{coh}})$ was used as a

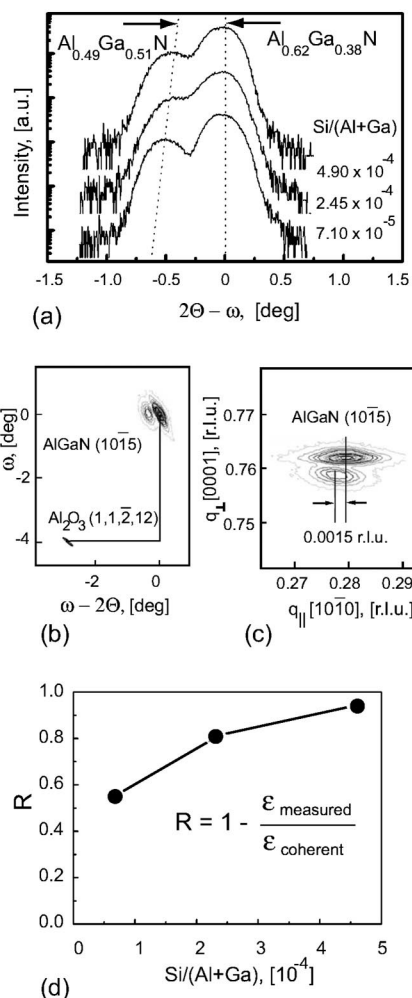


FIG. 3. HRXRD study of Si-doped $\text{Al}_{0.49}\text{Ga}_{0.51}\text{N}$ on $\text{Al}_{0.62}\text{Ga}_{0.38}\text{N}$ on Al_2O_3 samples. (a) X-ray ω - 2θ scans of Si-doped $\text{Al}_{0.49}\text{Ga}_{0.51}\text{N}$ on $\text{Al}_{0.62}\text{Ga}_{0.38}\text{N}$ samples showing the decreasing separation between the $\text{Al}_{0.49}\text{Ga}_{0.51}\text{N}$ (004) peak and the $\text{Al}_{0.62}\text{Ga}_{0.38}\text{N}$ (004) peak, with increasing $\text{Si}/(\text{Al}+\text{Ga})$. (b) Characteristic contour plot of a reciprocal space map used to determine the composition and strain state of the samples layers, where the Al_2O_3 $(1,1,\bar{2},12)$ reflection was used as angular reference. (c) Close-up of reciprocal space map near the asymmetric $(10\bar{1}5)$ reflection of the epilayer stack, showing how the stressed layer did not grow coherently on the buffer layer. (d) Extent of strain relaxation of the Si-doped $\text{Al}_{0.49}\text{Ga}_{0.51}\text{N}$ films, as determined from the analysis of the reciprocal space maps.

measure of the strain state of the epilayer,¹⁶ where ε_{coh} is the elastic strain in the fully coherent epitaxial layer (ε_{coh} is equal in magnitude to the crystal mismatch ε_m between the AlGaIn layers) and $\varepsilon_{\text{meas}}$ was the elastic strain value determined from the RSM analysis of the upper epilayer. The strain determined from the XRD data, $\varepsilon_{\text{meas}}$, was the elastic strain affecting the layer, and it was given by $\varepsilon_{\text{meas}} = \varepsilon_{\text{coh}} - \varepsilon_{\text{pl}}$, where ε_{pl} stands for the relaxed strain due to plastic deformation.

Following the procedure described above, we determined Al mole fractions of roughly $y=0.62$ for all buffer layers reported here, and the degree of stress relaxation was $R \approx 0.98$ or higher with respect to the sapphire substrate (note $R > 1$ corresponds to the generation of tensile stresses in the initially compressive layer). The residual strain on the $\text{Al}_{0.62}\text{Ga}_{0.38}\text{N}$ buffer layers was caused by strains associated

with the growth process, i.e., the lattice mismatch of 13.4% between the buffer and the sapphire, and the compressive thermal mismatch strain that developed while cooling to room temperature.⁹ The lattice mismatch between the $\text{Al}_{0.62}\text{Ga}_{0.38}\text{N}$ buffer layer and sapphire was relaxed by 98%. This extent of relaxation corresponds to a residual strain of approximately -0.27% (i.e., compressive) in the $\text{Al}_{0.62}\text{Ga}_{0.38}\text{N}$. The strain in the $\text{Al}_{0.62}\text{Ga}_{0.38}\text{N}$ layer due to thermal-expansion mismatch with the sapphire is estimated to be $\sim -0.30\%$. Thus, as the values of the measured residual strain in the $\text{Al}_{0.62}\text{Ga}_{0.38}\text{N}$ buffer layer at room temperature and the thermal strain were very close to each other, it is reasonable to assume that the $\text{Al}_{0.62}\text{Ga}_{0.38}\text{N}$ buffer layer was nearly completely relaxed with respect to the sapphire substrate during deposition of the Si-doped $\text{Al}_{0.49}\text{Ga}_{0.51}\text{N}$ layers.

Analysis of the Si-doped $\text{Al}_{0.49}\text{Ga}_{0.51}\text{N}$ layers was carried out using the methodology outlined for the buffer layers. Figure 3(c) shows a close-up of one RSM where it was apparent that the Si-doped $\text{Al}_{0.49}\text{Ga}_{0.51}\text{N}$ layer did not grow coherently on the underlying $\text{Al}_{0.62}\text{Ga}_{0.38}\text{N}$ buffer. In Fig. 3(c), “r.l.u.” refers to dimensionless reciprocal lattice units (λq). The rotation of the ellipses at half maximum intensity showed that the observed peak broadening was dominated by the lateral coherence length of the films and not by mosaic broadening.¹⁷ The analysis of the RSMs revealed that the Si-doped $\text{Al}_{0.49}\text{Ga}_{0.51}\text{N}$ films were partially relaxed with respect to the $\text{Al}_{0.62}\text{Ga}_{0.38}\text{N}$ buffer layers and the relaxation was more pronounced with a higher Si/(Al+Ga) ratio in the films. Figure 3(d) shows the dependence of the extent of stress relaxation of the $\text{Al}_{0.49}\text{Ga}_{0.51}\text{N}$ layers with respect to the $\text{Al}_{0.62}\text{Ga}_{0.38}\text{N}$ buffer layers on the Si/(Al+Ga) ratio. The stress relaxation increased monotonically from $R=0.55$, for a $\text{Si}/(\text{Al}+\text{Ga})=7.1 \times 10^{-5}$, to $R=0.80$ for a $\text{Si}/(\text{Al}+\text{Ga})=2.45 \times 10^{-4}$, to $R=0.94$ for a $\text{Si}/(\text{Al}+\text{Ga})=4.9 \times 10^{-4}$.

The relaxation results presented above have been observed on several experiments conducted before and after this study, where the Al mole fraction did not change by more than $\pm 1\%$ for films grown under identical conditions to those described above. In addition, Hall measurements conducted on these and similar Si-doped $\text{Al}_{0.49}\text{Ga}_{0.51}\text{N}$ samples grown at different times showed that the n -type conductivity also remained stable.¹⁸

C. Observation of inclined threading dislocations by TEM

TEM analysis of our samples showed that in the $\text{Al}_{0.62}\text{Ga}_{0.38}\text{N}$ buffer layers more than 90% of the TDs were pure edge dislocations with Burgers vector $\frac{1}{3}\langle 11\bar{2}0 \rangle$ and a line direction normal to the (0001) growth plane. Plan-view TEM images of an $\text{Al}_{0.62}\text{Ga}_{0.38}\text{N}$ buffer layer grown under identical conditions revealed an approximate TD density of $\rho_{\text{TD}} \sim 3 \times 10^{10} \text{ cm}^{-2}$.

Figures 4(a) and 4(b) show $\mathbf{g}=11\bar{2}0$ weak beam cross-section TEM images of samples where the $\text{Al}_{0.49}\text{Ga}_{0.51}\text{N}$ stressed layers were grown with $\text{Si}/(\text{Al}+\text{Ga})=7.1 \times 10^{-5}$ and $\text{Si}/(\text{Al}+\text{Ga})=4.9 \times 10^{-4}$, respectively. It is readily seen that the dislocations, which had a [0001] line direction in the buffer layers, were inclined in the stressed layers. The aver-

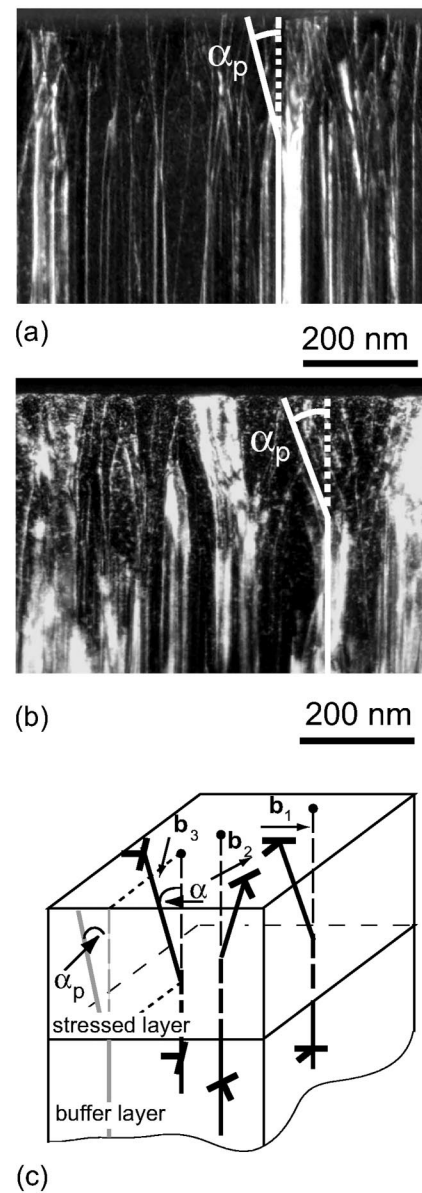


FIG. 4. Observation of inclined threading dislocations on $\text{Al}_{0.49}\text{Ga}_{0.51}\text{N}$ stressed films, via cross-section TEM images. (a) Cross-section $\mathbf{g}=11\bar{2}0$ weak beam dark-field image of the sample with the Si-doped $\text{Al}_{0.49}\text{Ga}_{0.51}\text{N}$ layer grown with $\text{Si}/(\text{Al}+\text{Ga})=7.1 \times 10^{-5}$. The projected inclination angle was $\alpha_p=15^\circ$, and the true inclination angle was $\alpha=17.2^\circ$. (b) Cross-section $\mathbf{g}=11\bar{2}0$ weak beam dark-field image of the sample with the Si-doped $\text{Al}_{0.49}\text{Ga}_{0.51}\text{N}$ layer grown with 4.9×10^{-4} . The projected TD inclination angle was $\alpha_p=20^\circ$, and the true TD inclination angle was $\alpha=22.8^\circ$. (c) Diagram depicting the three families of inclined edge dislocations in the stressed layer, which corresponded to the three possible orientations of the Burgers vector in the (0001) plane of the layer with a hexagonal crystal structure.

age projected angle of TD inclination, α_p , increased with $\text{Si}/(\text{Al}+\text{Ga})$ from $\alpha_p \sim 15^\circ$ for the sample shown in Fig. 4(a) to $\alpha_p \sim 20^\circ$ for the sample shown in Fig. 4(b). We refer to α_p as the “projected” inclination angle because, as will be shown later, the cross-section TEM images included a 30° projection of the inclined dislocations. Figure 4(c) shows a three-dimensional schematic of the inclined dislocations depicting the true angle of TD inclination, α .

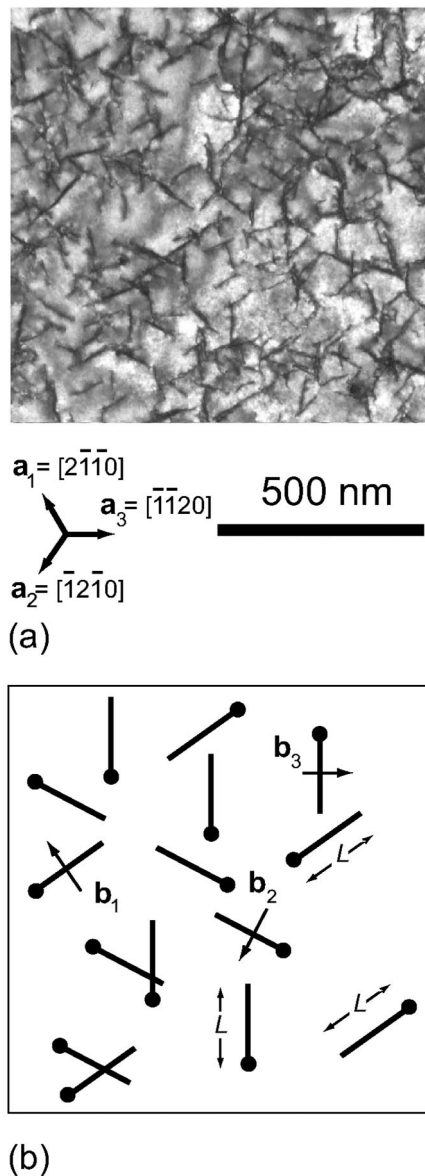


FIG. 5. Plan-view TEM analysis of $\text{Al}_{0.49}\text{Ga}_{0.51}\text{N}:\text{Si}$ films. (a) Plan-view TEM image of the $\text{Al}_{0.49}\text{Ga}_{0.51}\text{N}$ film grown with $\text{Si}/(\text{Al}+\text{Ga})=7.1 \times 10^{-5}$. The TDs are inclined toward the $\langle 1\bar{1}00 \rangle$ directions. (b) Plan-view diagram depicting the average dislocation projected length L , and the Burgers vectors of the edge dislocations showing that the inclined TDs maintain their pure edge character.

Figure 5(a) shows a plan-view TEM image taken in the $[0001]$ zone axis of the $\text{Al}_{0.49}\text{Ga}_{0.51}\text{N}$ stressed layer grown using $\text{Si}/(\text{Al}+\text{Ga})=7.1 \times 10^{-5}$. The thickness of the TEM sample was determined to be ~ 230 nm using a two-beam convergent beam electron-diffraction (CBED) patterns, and given that the stressed layer thickness was ~ 200 nm, it was reasonable to assume that all inclined dislocation segments should be visible. The analysis of this image (and a series of related images recorded under two-beam conditions, as shown below) showed that the TDs inclined toward the $\langle 1\bar{1}00 \rangle$ directions, e.g., TDs with Burgers vector $\mathbf{b} = \pm \frac{1}{3}[2\bar{1}\bar{1}0]$ inclined towards $\pm[0\bar{1}\bar{1}0]$ and thus maintain their pure edge character. When viewed along the growth direction, as shown schematically in Fig. 5(b), the inclined

TDs had an average projected length L on the (0001) plane, i.e., for the sample shown in Fig. 5(a) we measured $L = 80$ nm. In the far field, the projected dislocation lines are equivalent to effective MD segments. Therefore, L also stands for the effective MD length. Also on Fig. 5(b), the dots indicate the initial position of the TDs before inclination, i.e., in the buffer layer.

The true angles of TD inclination, α , for the samples shown in Figs. 4(a) and 4(b) could then be calculated, given that the $[10\bar{1}0]$ -oriented cross-section TEM samples gave a 30° projection of the $\{11\bar{2}0\}$ planes along which the TDs were inclined. Therefore, for the sample grown with $\text{Si}/(\text{Al}+\text{Ga})=7.1 \times 10^{-5}$, shown in Fig. 4(a) with $\alpha_p \sim 15^\circ$ corresponded to $\alpha \sim 17^\circ$, while for the sample with $\text{Si}/(\text{Al}+\text{Ga})=4.9 \times 10^{-4}$, shown in Fig. 4(b) with $\alpha_p \sim 20^\circ$ corresponded to $\alpha \sim 23^\circ$. From these angles we calculated the MD length of the inclined TDs by noting that $L = h \tan \alpha$, where h is the stressed layer thickness, resulting in $L = 62$ nm and $L = 85$ nm for the samples in Figs. 4(a) and 4(b), respectively.

We have performed systematic zone-axis and two-beam studies on plan-view samples to determine the line direction and Burgers vectors of the inclined TDs. Figure 6(a) shows a $[0001]$ zone-axis image of a partially relaxed $\text{Al}_{0.49}\text{Ga}_{0.51}\text{N}$ buffer and Figs. 6(b) and 6(c) show two-beam images recorded with $\mathbf{g} = 1\bar{2}10$ and $\mathbf{g} = 10\bar{1}0$, respectively. The zone-axis diffraction pattern is inset in Fig. 6(a) and shows the six equivalent $\{10\bar{1}0\}$ reflections. The nearly vertical dislocations in the figure have a projected line direction of $[10\bar{1}0]$. The $\mathbf{g} = 1\bar{2}10$ two-beam image in Fig. 6(b) shows that the TDs with projected $[10\bar{1}0]$ direction are in strong contrast whereas the $\mathbf{g} = 10\bar{1}0$ two-beam image in Fig. 6(c) shows these TDs to be out of contrast. Based on standard $\mathbf{g} \cdot \mathbf{b}$ analysis, these results demonstrate that the Burgers vector for the TDs with the $[10\bar{1}0]$ projected line direction is $\mathbf{b} = \pm \frac{1}{3}[1\bar{2}\bar{1}0]$ and thus the TDs inclined in a sense that maintains their pure edge character.

It will be shown in the Discussion that the effective MD segments of the inclined TDs were responsible for the partial relaxation of the Si-doped AlGaN films. For reference, the degree of stress relaxation at the stressed layer surface, R_{surf} , calculated from the TEM results, was $R_{\text{surf}}=0.84$ and $R_{\text{surf}}=1.09$ for the samples grown with $\text{Si}/(\text{Al}+\text{Ga})=7.1 \times 10^{-5}$ and $\text{Si}/(\text{Al}+\text{Ga})=4.9 \times 10^{-4}$, respectively, which is in good agreement with the ones obtained from the analysis of the XRD data.

IV. MODELING

For modeling considerations, we assume that the majority of the TDs had a pure edge character with Burgers vector of the type $\frac{1}{3}\langle 11\bar{2}0 \rangle$ and dislocation density was greater than 10^{10} cm^{-2} . In the buffer layer these TDs have a $[0001]$ line direction; however, in the stressed layer the dislocations change their line orientation, with respect to the growth direction, by inclination angles α as large as 23° , as shown schematically in Fig. 4(c). As described in the Experiment

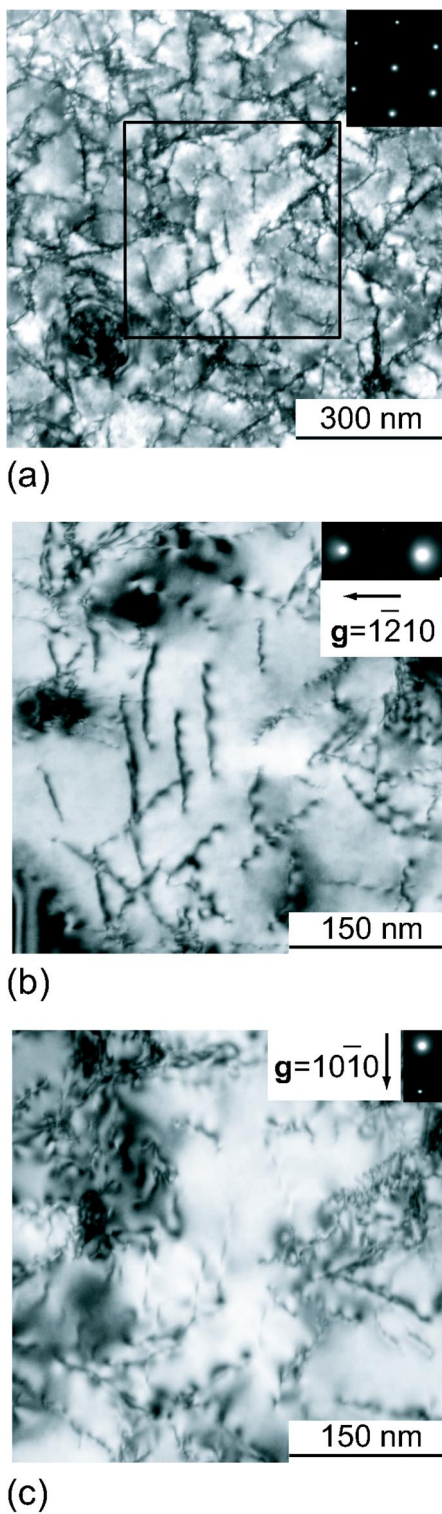


FIG. 6. Plan-view TEM images of a partially relaxed $\text{Al}_{0.49}\text{Ga}_{0.51}\text{N}$ buffer layer: (a) $[0001]$ zone-axis image with inset diffraction pattern. The square denotes the area for imaging in (b) and (c); (b) $\mathbf{g}=1\bar{2}10$ two-beam image; (c) $\mathbf{g}=10\bar{1}0$ two-beam image. The nearly vertical TDs in this image have a $[10\bar{1}0]$ projected line direction and Burgers vector $\mathbf{b}=\pm\frac{1}{3}[\bar{1}2\bar{1}0]$.

section, plan-view TEM studies showed that the TDs were inclined toward the $\langle 1\bar{1}00 \rangle$ directions, therefore maintaining their pure edge character.

Since the TDs inclined toward one of the six $\langle 1\bar{1}00 \rangle$ directions in the Si-doped layers, we assume for modeling

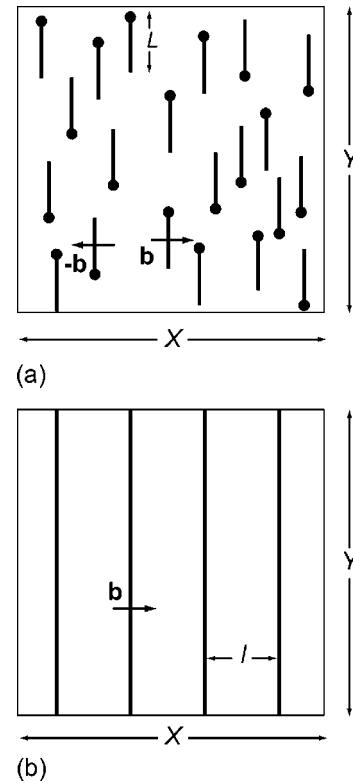


FIG. 7. Equivalency between the effective misfit dislocations considered in the model and a single family of inclined dislocations. (a) Plan-view diagram for a selected family of inclined dislocations with an average projected length L per dislocation and total length Λ . (b) Plan-view diagram of the equally spaced misfit dislocation with the same total length Λ .

purposes that the total density of TDs was equally partitioned among these six directions. Accounting for the possible sense of the Burgers vectors, we treat three distinguishable families of TDs, where for each family $\rho_1 = \frac{1}{3}\rho_{\text{TD}}$. Throughout this treatment we assign the line direction of the TDs to be in the same sense as the outward normal to the free surface of the upper layer. We then consider one particular family, as shown schematically in Fig. 7(a). For this family, dislocations with opposite Burgers vectors (\mathbf{b} and $-\mathbf{b}$) incline in opposite directions [Fig. 7(a)] to provide the same sense of misfit strain relief. To simplify our analysis, we consider that all MD segments for each family had the same Burgers vector and inclined in the same direction. We could then hypothetically combine the MD segments to form straight-line MD arrays with a distance l between MDs, as shown in Fig. 7(b). To determine l we first note that the total projected length of effective MDs in an area with dimensions X and Y is

$$\Lambda = \rho_1 XY L. \quad (1)$$

Then the distance between effective straight MDs in the array is

$$l = \frac{X}{(\Lambda/Y)} = \frac{1}{\rho_1 L}. \quad (2)$$

The plastic relaxation associated with such an array of effective MDs could then be given simply as

$$\varepsilon_{pl}^1 = \frac{b}{l} = b\rho_{TD}L = \frac{1}{3}b\rho_{TD}L, \quad (3)$$

where b is the magnitude of the Burgers vector of the family of dislocations. Equation (3) accounts for the one-dimensional plastic deformation along the direction perpendicular to the MD lines. It can be shown¹⁹ that the resulting triangular crossgrid of MD line arrays produces equibiaxial far-field plastic relaxation ε_{pl}^{top} at the top layer surface, given by

$$\varepsilon_{pl}^{top} = \frac{3}{2}\varepsilon_{pl}^1 = \frac{1}{2}b\rho_{TD}L. \quad (4)$$

Because the TDs inclined at the stressed layer/buffer layer interface, the effective MD length, L , is directly related to the stressed layer thickness h and the inclination angle α by $L = h \tan \alpha$. This also means that the MD length varied linearly with layer thickness, thus providing a plastic strain gradient given by

$$\frac{d\varepsilon_{pl}}{dz} = \frac{1}{2}b\rho_{TD} \tan \alpha. \quad (5)$$

The linear strain gradient leads to an average plastic relaxation of the stressed layer of thickness h , given by

$$\bar{\varepsilon}_{pl} = \frac{1}{4}b\rho_{TD}h \tan \alpha. \quad (6)$$

To analyze the conditions for TD inclination in a stressed layer, we consider an energy balance similar to the ‘‘energy approach’’ for deriving the critical thickness for MD generation in stressed films.^{20,21} We consider two configurations for the initially stressed layer with a single dislocation: (i) the misfitting layer with a straight edge dislocation with a line direction normal to the layer surface; and (ii) the misfitting layer with an inclined edge dislocation [assuming that the dislocation only inclined in the misfitting layer, as shown in Fig. 8(a)].

First, we assume that the top layer has a nominal compressive biaxial stress, σ , given by

$$\sigma_{xx} = \sigma_{yy} = \sigma = 2G \frac{1 + \nu}{1 - \nu} \varepsilon_m, \quad (7)$$

where $\varepsilon_m = \varepsilon_{coh}$ was the crystal lattice mismatch between the buffer and the layer, G is the shear modulus, and ν is Poisson's ratio.

The energy of the first state E_i is given as

$$E_i = E_{straight} + E_{biaxial} - W_{int}^i, \quad (8)$$

where $E_{straight}$ is the self-energy of the dislocation in the initial configuration with its line direction normal to the surface, $E_{biaxial}$ is the energy of the biaxial stress, and W_{int}^i is the interaction energy between biaxial stress and straight threading dislocation. W_{int}^i can be calculated as the work done by the biaxial misfit stress σ in the process of introducing the threading dislocation into the material (work of plastic deformation), and therefore depends on the history of this plastic deformation.

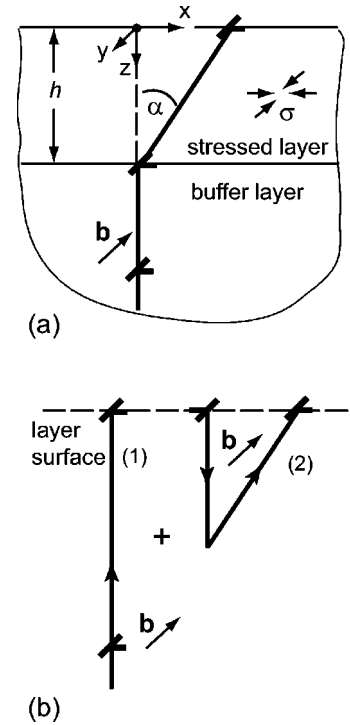


FIG. 8. Inclined dislocation represented as a superposition of a straight dislocation and an angular dislocation. (a) Inclined dislocation with Burgers vector b in the yz plane. (b) Schematic of a straight (i) and an angular (ii) dislocation with the same Burgers vector b .

The energy of the second state E_{ii} is defined in a similar way,

$$E_{ii} = E_{inclined} + E_{biaxial} - W_{int}^{ii}, \quad (9)$$

where the terms have a similar meaning as in Eq. (8) and $E_{inclined}$ is the self-energy of the dislocation in the inclined configuration.

Then, the energy release ΔE due to dislocation inclination is given as

$$\Delta E = E_{ii} - E_i = E_{inclined} - E_{straight} - \Delta W_{int}, \quad (10)$$

where $\Delta W_{int} = W_{int}^{ii} - W_{int}^i$ is the work done by the biaxial misfit stress σ in the process of dislocation inclination (note that in our previous work¹³ we used a different designation for ΔW_{int}).

To determine $E_{inclined}$, as shown in Fig. 8(b), the inclined dislocation is modeled as the superposition of a straight dislocation (1) and an angular dislocation (2). In this case, $E_{inclined}$ is given by

$$E_{inclined} = E_{straight} + E_{angular} + W_{straight}^{angular}, \quad (11)$$

where $E_{angular}$ is the self-energy of the angular dislocation and $W_{straight}^{angular}$ is the interaction energy with the initial dislocation.

The precise analysis of the terms involved in Eq. (11) is based on the solution of the boundary-value problem in the theory of elasticity for an angular dislocation in a subsurface layer. The technique used to determine the angular dislocation elastic field involves the integration of known stresses of infinitesimally small prismatic dislocation loops²² over the area of the angular dislocation.¹⁹ Subsequently, integration of

the elastic field yielded the elastic self-energy term in Eq. (11). Exact calculations of the energy E_{angular} must include the contribution of the dislocation core region (which is proportional to the change in dislocation length). The results of such analysis will be reported elsewhere.¹⁹ Numerical estimates showed that the interaction contribution, $W_{\text{straight}}^{\text{angular}}$, canceled in the first approximation when considering the dislocation core contribution. As a result the energy balance has a simpler form:

$$\Delta E = E_{\text{angular}} - \Delta W_{\text{int}}. \quad (12)$$

The interaction part is given as

$$\Delta W_{\text{int}} = b\sigma S_{\text{angular}} = G \frac{1+\nu}{1-\nu} b h^2 \varepsilon_m \tan \alpha, \quad (13)$$

where S_{angular} is the area bounded by the angular dislocation. Note that in the derived form of the energy release, we avoid the use of such undefined and formally infinite terms as the self-energy of the straight dislocation E_{straight} , the elastic energy of the stressed layer E_{biaxial} , and the interaction energies W_{int}^i and W_{int}^{ii} .

Here we use an approximate expression for E_{angular} developed in Ref. 19, based on the physical arguments of varying screening length, R_s , for the dislocation elastic field in the process of TD inclination. For small inclination angles, the angular dislocation is equivalent to the edge dipole with a separation of the order $h \sin \alpha \approx h\alpha$. Therefore, the screening length could be taken as $R_s = h \sin \alpha$. For large inclinations ($\alpha \rightarrow \pi/2$), the dislocation acquired a parallel orientation with respect to the layer surface and the characteristic screening length is then just the layer thickness $R_s = h$. Accordingly, the dislocation length changed as $h/\cos \alpha$ with inclination α . These observations led us to the following dependence for E_{angular} :

$$E_{\text{angular}} = \frac{Gb^2}{4\pi(1-\nu)} \frac{h}{\cos \alpha} \log \left[\left(\frac{h}{b} - 1 \right) \sin \alpha + 1 \right], \quad (14)$$

where we use b for the dislocation core radius. The numerical calculations obtained in the framework of the exact solution demonstrated that the proposed form of Eq. (14) gave a good approximation for E_{angular} over a wide range of film thicknesses and inclination angles.

Finally, we analyze the following dependence for the energy release:

$$\Delta E(h, \alpha) = \frac{Gb^2}{(1-\nu)} \left\{ \frac{h}{4\pi \cos \alpha} \log \left[\left(\frac{h}{b} - 1 \right) \sin \alpha + 1 \right] - (1+\nu) \frac{h^2}{b} \varepsilon_m \tan \alpha \right\}. \quad (15)$$

A typical dependence for ΔE is shown in Fig. 9(a). It is clear that for sufficiently large stressed layer thickness or TD inclination angle α , ΔE became negative, which demonstrate the favorable conditions for plastic relaxation via TD inclination. By requiring that $\Delta E=0$, we map the regions for favorable dislocation inclination in coordinates layer thickness versus inclination angle, as shown in Fig. 9(b). The plots define the energetic conditions for dislocation inclination for a given misfit strain. Also, when $\alpha \rightarrow \pi/2$, the plots

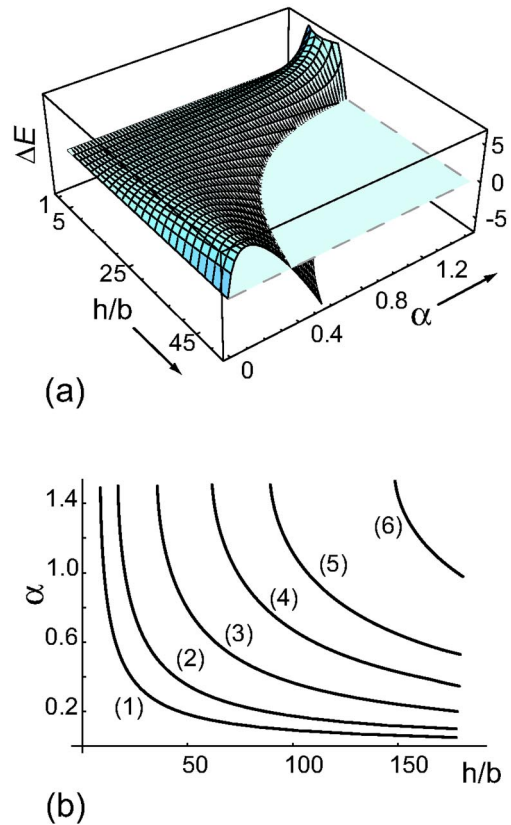


FIG. 9. Critical conditions for edge dislocation inclination in the stressed layer. (a) Energy release due to the inclination of the initially straight edge dislocation. Parameters used for the plot: misfit strain in the layer $\varepsilon_m = 0.01$, dislocation core radius $R_c = b$, and Poisson ratio $\nu = 1/3$. The energy change ΔE is given in units of Gb^3 . (b) Inclined edge dislocation stability diagram, given as layer thickness h vs inclination angle α , for misfit strains $\varepsilon_m = 0.015$ (1), 0.010 (2), 0.006 (3), 0.004 (4), 0.003 (5), and 0.002 (6), respectively.

demonstrate the usual critical thickness behavior for MD formation in mismatched layers.

V. DISCUSSION

The partial stress relaxation observed for Si-doped $\text{Al}_{0.49}\text{Ga}_{0.51}\text{N}$ films, as shown in Fig. 3(c), was attributed to the relaxation of misfit strain in the stressed layer via TD inclination. Under this assumption, the strain measured by HRXRD was the residual strain in the film after plastic relaxation or $\varepsilon_{\text{mes}} = \varepsilon_{\text{coh}} - \varepsilon_{\text{pl}}$, and the degree of stress relaxation defined previously has the form

$$R = 1 - \frac{\varepsilon_{\text{mes}}}{\varepsilon_{\text{coh}}} = \frac{\varepsilon_{\text{pl}}}{\varepsilon_m}. \quad (16)$$

As stipulated in the Modeling section, the inclined dislocations generated a strain gradient [Eq. (5)]. However, as we measured the strain state of the samples via HRXRD, it is reasonable to assume that the x-ray experiments average over the full-strained layer thickness. Instead, using Eq. (4) we calculated the plastic relaxation at the surface of the samples shown in Figs. 4(a) and 4(b) from TEM results, given that $\rho_{\text{TD}} \approx 3 \times 10^{10} \text{ cm}^{-2}$, $h = 200 \text{ nm}$, $b = 0.318 \text{ nm}$, and the initial misfit between the stressed and buffer layers was ε_{coh}

=0.0032. For the $\text{Al}_{0.49}\text{Ga}_{0.51}\text{N}$ layer grown using a $\text{Si}/(\text{Al}+\text{Ga})=7.1 \times 10^{-5}$, shown in Fig. 4(a), we calculate $\epsilon_{\text{pl}}^{\text{top}}=0.0029$, while for the layer with $\text{Si}/(\text{Al}+\text{Ga})=4.9 \times 10^{-4}$, shown in Fig. 4(b), we obtained $\epsilon_{\text{pl}}^{\text{top}}=0.0040$, which resulted in degrees of stress relaxation at the surface of $R^{\text{top}}=0.92$ and $R^{\text{top}}=1.25$, respectively.

These results were in good agreement with the HRXRD observation that with increasing $\text{Si}/(\text{Al}+\text{Ga})$, from 7.1×10^{-5} to 4.9×10^{-4} , the stress relaxation increased, from $R=0.55$ to $R=0.94$, as seen in Fig. 3(c) given that the TEM analysis relied on the estimated values for the TD density, and the inclination angles were obtained from images covering limited areas of the samples.

We have developed a theoretical framework to explain the TD inclination. We employed an energy balance method that measured the energetic difference between two possible TD states (straight dislocation and inclined dislocation), which determines the necessary conditions for the onset of TD inclination, $\Delta E(h, \alpha) \leq 0$. It was found that for a sufficiently thick stressed layer ΔE became negative, therefore favoring plastic relaxation via TD inclination. This also occurred for large values of possible inclination angles α . The energetic conditions were easier to achieve for layers with large initial misfit strain with respect to their underlayer. For $\alpha \rightarrow \pi/2$ corresponds to the usual critical thickness behavior for MD formation in mismatched layers. The other important feature revealed by the $\Delta E(h, \alpha)$ dependence is the existence of an energy barrier to dislocation inclination at finite values of the stressed layer thickness h . The typical heights for this barrier are $\sim 5-10 \text{ Gb}^3$, which leads to reasonable values of 10 eV per dislocation. To overcome these barriers additional factors should be considered.

According to our observations, the TD inclination angle α was effected by the DiSi injection during growth of the samples, because all other growth parameters were nominally identical in our growth experiments. The antisurfactant effect of Si on nitride films generated an increased surface roughness that had a definite correlation with increased stress relaxation of the Si-doped layers, as seen by comparing Figs. 2(b) and 3(c). We believe that the surface roughness of the stressed layer during growth helped diminish the energy barrier during the initial stage of TD inclination. These ideas are consistent with the models proposed for dislocation nucleation during the development of morphological instabilities at the stressed surfaces of crystals.^{23,24}

Once inclined, the TDs maintained their orientation, i.e., the TD line direction became frozen in and thus demonstrated that dislocation climb did not occur in the bulk of the material. Although we recognize that our claim of no bulk dislocation climb occurs during the growth of the AlGaIn layers is a conjecture, there are few, if any, conclusive reports of dislocation climb in GaN layers. The possible mechanisms of epitaxial growth with inclined threading dislocations may include directional surface diffusion and/or the incorporation of adatoms at the intersection of preexisting TDs with the growing crystal surface. Due to this behavior, we refer to this mechanism as an “effective climb” process. A schematic showing the onset and further propagation of an inclined dislocation is shown in Fig. 10. However, new mod-

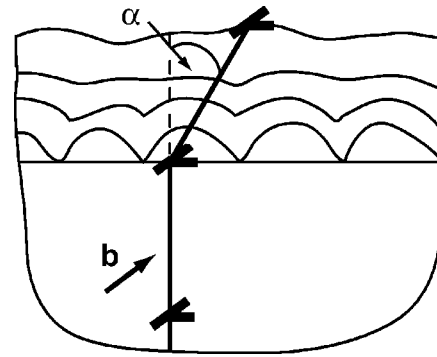


FIG. 10. Schematic of a bended threading dislocation: inclination onset and further propagation. The TD line direction changed abruptly at the roughened surface, and then it maintained its new line direction “propagating” laterally with increasing film thickness.

els that detail the effective climb process should be developed. These models should account for both local surface morphology and the role of adatom interaction with the region near the TD intersection with the free surface.

We note that the strain gradient given by Eq. (5) dependent only on the dislocation density and the inclination angle, not on the layer thickness. This may lead to a sign change of the stresses with increased layer thickness. Consider, for example, a nominally compressed layer, which becomes stress-free due to inclined dislocations at the particular thickness h_f . If the dislocations maintain their inclination, the stress on the film would go from compressive to tensile when growth of the stressed layer continued for thicknesses above h_f . We have observed cracking of nominally compressively strained layers and attributed the cracking to the development of tensile stresses from inclined TDs.²⁵

VI. SUMMARY AND CONCLUSIONS

We have experimentally established that increased $\text{Si}/(\text{Al}+\text{Ga})$ during deposition enhanced the stress relaxation of nominally compressed $\text{Al}_{0.49}\text{Ga}_{0.51}\text{N}$ films grown on top of $\text{Al}_{0.62}\text{Ga}_{0.38}\text{N}$ buffer layers. The partial relaxation of the stressed films was associated with the inclination of threading dislocation lines with respect to the growth direction, generating effective misfit dislocation segments that released initially compressive stresses in the layers. We have realized good agreement between the degrees of strain relaxation determined from HRXRD and from TEM. The redirection of threading dislocation lines has been associated with Si-induced surface roughness during growth.

The model developed here provides a set of conditions for the onset of threading dislocation inclination, which were large stressed layer thicknesses and/or large inclination angles. In the limit when the threading dislocation inclination angle tended to 90° , the modeled behavior confirmed the expected misfit dislocation generation conditions with increasing thickness. It was also found that for thin stressed films an energy barrier of up to 10 eV existed for the dislocation inclination to occur. However, we believe that the surface roughness may reduce this barrier, thus allowing for the

inclination of preexisting threading dislocations. The inclined threading dislocations relieve the stress of the mismatched layers.

ACKNOWLEDGMENTS

This work was supported by DARPA (J. Carrano, program manager). One of the authors (P.C.) acknowledges the support of CoNaCyT and UCMexus. The work of another author (F.W.) was supported by the JST/ERATO program at UCSB.

¹L. Coldren and S. W. Corzine, in *Diode Lasers and Photonic Integrated Circuits*, Wiley Series in Microwave and Optical Engineering, edited by K. Chang (Wiley Interscience, New York, 1995), Chap. 4.

²L. B. Freund, *MRS Bull.* **17**, 52 (1992).

³J. W. Matthews and A. E. Blakeslee, *J. Cryst. Growth* **27**, 118 (1974).

⁴I. Lee *et al.*, *J. Appl. Phys.* **83**, 5787 (1998).

⁵S. Ruvimov *et al.*, *Appl. Phys. Lett.* **69**, 990 (1996).

⁶L. T. Romano, C. G. Van de Walle, J. W. Ager III, W. Götz, and R. S. Kern, *J. Appl. Phys.* **87**, 7745 (2000).

⁷R. W. Hoffmann, *Phys. Thin Films* **3**, 211 (1966).

⁸W. D. Nix and B. M. Clemens, *J. Mater. Res.* **14**, 3467 (1999).

⁹T. Böttcher, S. Einfeldt, S. Figge, R. Chierchia, H. Heinke, D. Hommel,

and J. S. Speck, *Appl. Phys. Lett.* **78**, 1976 (2001).

¹⁰S.-L. Sahonta, M. Q. Baines, D. Cherns, H. Amano, and F. A. Ponce, *Phys. Status Solidi B* **234**, 952 (2002).

¹¹P. Cantu, F. Wu, P. Waltereit, S. Keller, A. E. Romanov, U. K. Mishra, S. P. DenBaars, and J. S. Speck, *Appl. Phys. Lett.* **83**, 674 (2003).

¹²S. Keller, P. Waltereit, P. Cantu, U. K. Mishra, J. S. Speck, and S. P. DenBaars, *Opt. Mater. (Amsterdam, Neth.)* **23**, 187 (2003).

¹³A. E. Romanov and J. S. Speck, *Appl. Phys. Lett.* **83**, 2569 (2003).

¹⁴S. Keller, U. K. Mishra, S. P. DenBaars, and W. Seifert, *Jpn. J. Appl. Phys., Part 2* **37**, L431 (1998).

¹⁵A. Munkholm *et al.*, *Appl. Phys. Lett.* **77**, 1626 (2000).

¹⁶O. Brandt, P. Waltereit, and K. H. Ploog, *J. Phys. D* **35**, 577 (2002).

¹⁷R. Chierchia, T. Böttcher, H. Heinke, S. Einfeldt, S. Figge, and D. Hommel, *J. Appl. Phys.* **93**, 8918 (2003).

¹⁸P. Cantu, S. Keller, U. K. Mishra, and S. P. DenBaars, *Appl. Phys. Lett.* **82**, 3683 (2003).

¹⁹A. E. Romanov and J. S. Speck, *Appl. Phys. Lett.* **83**, 2569 (2003).

²⁰V. I. Vladimirov, M. Y. Gutkin, and A. E. Romanov, *Poverkhnost* **6**, 46 (1988).

²¹J. R. Willis, S. C. Jain, and R. Bullough, *Philos. Mag. A* **62**, 115 (1990).

²²P. P. Groves and D. J. Bacon, *Philos. Mag.* **16**, 83 (1970).

²³J. Grilhe, *Europhys. Lett.* **23**, 141 (1993).

²⁴H. Gao, *J. Mech. Phys. Solids* **42**, 741 (1994).

²⁵P. Cantu, F. Wu, A. E. Romanov, S. P. DenBaars, and J. S. Speck (unpublished).